ADVANCED FUNCTIONAL MATERIALS
www.afm-journal.de

Tissue-Adhesive Piezoelectric Soft Sensor for In Vivo Blood Pressure Monitoring During Surgical Operation

Chan Wang, Yiran Hu, Ying Liu, Yizhu Shan, Xuecheng Qu, Jiangtao Xue, Tianyiyi He, Sijing Cheng, Hong Zhou, Weixin Liu, Zi Hao Guo, Wei Hua, Zhuo Liu, Zhou Li,* and Chengkuo Lee**

The reliable function in vivo of self-powered implantable bioelectric devices (iBEDs) requires biocompatible, seamless, effective interactions with biological tissues. Herein, an implantable tissue-adhesive piezoelectric soft sensor (TPSS), in which the piezoelectric sensor converts biomechanical signals into electrical signals, and the adhesive hydrogel (AH) strengthens this conversion by seamlessly adhering the sensor on the wet and curvilinear surface, is proposed. The optimized AH exhibits strong adhesion to various organic or inorganic surfaces, including six commonly used engineering materials and three biological tissues. As a pressure sensor, TPSS proves good in vitro electrical performance with a high output of 8.3 V, long-term stability of over 6000 cycles, and high energy power density of 186.9 μW m^{-2}. In a large animal experiment, TPSS seamlessly adheres to the right-side internal carotid artery of a Yorkshire pig to monitor blood pressure during a surgical operation. Compared to commercial sensors that work by inserting into tissues, TPSS does not cause any damage and can be peeled off after service. The integration of adhesive hydrogel and self-powered pressure sensors enables biocompatible, seamless, and more efficient interactions between the biological system and iBEDs, which also contributes to next-generation implantable bioelectronics with features of battery-free, intelligent, and accurate.

1. Introduction

Biomedical electronic devices (BED) are interfaced with the human body in wearable or implantable ways to extract precise medical data or intervene in tissue functions.[1] Wearable BEDs derive physiological signals from the skin surface or areas close to the epidermis (≈mm) by measuring body movement, respiration, sweetness, temperatures et al.[1b,2] On the other hand, the physiological status of organs or tissues, which are closely related to disease, are available to implantable biomedical electronic devices (iBEDs).[1a,3] Since the first implanted cardiac pacemaker, advances in micro/nanoelectronics fabrication technologies and multifunctional materials pushing iBEDs toward ultralow power consumption, miniaturization, and intelligence.[4] The proposal of self-powered technologies represented by triboelectric nanogenerators (TENG)[5] and piezoelectric nanogenerators (PENG) free iBEDs from the shackles of massive and limited-life batteries.[1d,2b,5d,6] The first

C. Wang, T. He, H. Zhou, W. Liu, C. Lee
Department of Electrical & Computer Engineering
Center for Intelligent Sensors and MEMS (CISM)
National University of Singapore
Singapore 117583, Singapore
E-mail: elelc@nus.edu.sg

C. Wang, T. He, H. Zhou, W. Liu, C. Lee
Centre for Peak of Excellence on Smart Medical Technology
National University of Singapore Suzhou Research Institute (NUSRI)
Suzhou 215123, China

Y. Hu, S. Cheng, W. Hua
The Cardiac Arrhythmia Center, State Key Laboratory of Cardiovascular Disease, National Clinical Research Center of Cardiovascular Diseases, Fuwai Hospital, National Center for Cardiovascular Diseases
Chinese Academy of Medical Sciences and Peking Union Medical College
Beijing 100037, China

Y. Hu
Department of Cardiology and Macrovascular Disease, Beijing Tiantan Hospital
Capital Medical University
Beijing 100070, China

Y. Liu, Y. Shan, X. Qu, J. Xue, Z. H. Guo, Z. Liu, Z. Li
School of Nanoscience and Technology
University of Chinese Academy of Sciences
Beijing 100049, China
E-mail: liuzhuo@binn.cas.cn; zli@binn.cas.cn

Y. Liu, Y. Shan, X. Qu, J. Xue, Z. H. Guo, Z. Liu, Z. Li
Beijing Institute of Nanoenergy and Nanosystems
Chinese Academy of Sciences
Beijing 101400, China

Z. Liu
Key Laboratory of Biomechanics and Mechanobiology of Ministry of Education, Advanced Innovation Center for Biomedical Engineering, School of Engineering Medicine
Beihang University
Beijing 100191, China

The ORCID identification number(s) for the author(s) of this article can be found under https://doi.org/10.1002/adfm.202303696

DOI: 10.1002/adfm.202303696

TENG-based iBED was designed to harvest energy in a living rat.[7] After that, more successors demonstrated their extraordinary abilities in cardiovascular disease monitoring and direct electrical stimulation for treating neurological diseases. Meanwhile, with the advantages of lightweight, low cost, and high output energy density, PENG-based iBEDs stand out. A two-ends-bonded single ZnO nanowire on a flexible substrate was fabricated as an alternating nanogenerator to convert biomechanical energy from a live rat's breath and heartbeat into an electrical signal.[8] On this basis, self-powered iBEDs with extra characteristics of good degradability,[4a,9] self-healing, and antibacterial[10] were furtherly reported, which made applications in vivo energy harvesting,[11] cardiovascular monitoring,[4a,12] cardiac pacing,[13] muscle/nerve electrical stimulation,[14] tissue regeneration,[15] and drug delivery.[16]

Despite the above advances, developing efficient, seamless communication, and interactions between iBEDs and tissues is still largely primitive. Existing iBEDs are mainly prepared from hard, dry, and abiotic materials, such as elastomers, plastics, metal, and silicon,[12,17] which are inherently incompatible with the soft, wet, and living biological tissues.[3b,18] For example, traditional nerve probes and arrays in neuroscientific explorations, such as Michigan probes and Utah arrays, normally cause adverse foreign body reactions resulting in gliosis and fibrosis, which seriously hinder the reliability and functionality of implants.[19] In parallel, the soft and curvilinear surfaces of biological tissues should be taken into consideration. Extensive efforts in establishing conformal contact with tissue were invested by endowing traditional materials with flexible and stretchable structures, such as wavy shapes and mesh designs.[20] However, these strategies did not improve the intrinsic modulus mismatch between iBEDs and biological tissues. We summarized the research progress of iBEDs in terms of device-tissue interfaces, device design, and performance, et al., please find more details in Table S1 (Supporting Information). Currently, integrating self-powered iBEDs with biological tissue mainly relies on physical attaching, gluing, and surgical suturing (Figure S1, Supporting Information). These methods are nonconformal, not stable, or will damage surrounding tissues.

Adhesive hydrogels emerged as a versatile candidate in bridging the iBEDs and biological tissues with their special similarities to biological tissues.[1a,21] Adhesive hydrogels are hydrophilic 3D polymer networks that contain tissue-like high water content, which closely mimics physiological environments and minimizes potential problems induced by implanted foreign bodies.[19a,21a,22] The Young's modulus of adhesive hydrogels is ranging from pascal (Pa) to megapascal (MPa), which is well matched with biological tissues.[1a,23] This enables adhesive hydrogels to form seamless conformal contact with curvilinear physiological surfaces. Although, efforts were made to design adhesive hydrogels used as epidermal electrodes, immobilize implants, sealants, and surgical instruments coats.[15b,19a,24] These adhesive hydrogels usually require surface polar treatment of targets, otherwise, the adhesion efficiency will greatly reduce. In nature, mussels can tightly cling to reefs under seawater, relying on the adhesive proteins secreted by their byssus.[25] These mussel adhesive proteins (MAPs) contain abundant catechol groups, which enable strong adhesion with various organic and inorganic surfaces through forming charge–charge interactions, covalent bonds, hydrogen bonds, and Π–Π bonds (Figure S2, Supporting Information).[25] Taking full consideration of the biocompatibility and wet adhesive characteristic, MAPs inspire the hydrogel design for facilitating efficient and seamless interactions between iBEDs and biological tissues.

In this paper, we propose a tissue-adhesive piezoelectric soft sensor (TPSS) for in vivo monitoring, in which a piezoelectric sensor converts biomechanical movements into electrical signals, and the adhesive hydrogel (AH) strengthens this conversion by seamlessly adhering the sensor on the wet and curvilinear surface of biological tissues. The soft sensor is fabricated using piezoelectric polyvinylidene fluoride (PVDF) film in β phase, which was sensitive to continued dynamic bending. The AH is designed based on biologically derived MAPs and gelatin, behaving strong adhesion to 6 commonly used engineering materials (including polyimide, rubber, polycarbonate, polymethyl methacrylate, titanium, and copper) and 3 biological tissues (kidney, skin, and heart). The tunable Young's modulus, good biocompatibility, and superior adhesion performance prove the potential of AH in bridging iBEDs and biological tissues. As a pressure sensor, TPSS can seamlessly adhere to the artery of a Yorkshire pig to monitor intraoperative vital indicators, such as blood pressure, heart rate, and respiratory rate. After service, TPSS is easily peeled off without damaging surrounding tissues. The integration of adhesive hydrogel and self-powered pressure sensor enabled the biocompatible, seamless, and more efficient interactions between the biological system and iBEDs, which also provided reference to next-generation implantable bioelectronics with features of battery-free, intelligent, and accurate.

2. Results and Discussion

2.1. Overview of the Tissue-Adhesive Piezoelectric Soft Sensor (TPSS)

The design principles of TPSS were displayed in **Figure 1**. There are two parts consisting of TPSS, the adhesive hydrogel (AH), and the piezoelectric sensor. To realize both strong adhesion and good biocompatibility, MAPs derived from mussel byssus and gelatin from porcine skin were selected to design AH through a simple one-step method (Figure 1a). In brief, AH was fabricated by dissolving proportioned components into deionized water, followed by 2 h of polymerization under ultraviolet (UV) light. More details could be found in the Experimental Section. The size and thickness of AH film could be customizable by altering the parameters of glass molds used in polymerization. Figure S3 (Supporting Information) displayed a dehydrated AH film in size of 10✗10 cm^2, in thickness of ≈40 μm. The as-fabricated AH performed strong adhesion to both biological interfaces (like skin) and inorganic interfaces (like metal), where no pretreatment or surface modification was required (Figure 1b,c). Five layers consisted of the piezoelectric soft sensor, as shown in Figure 1d,e, including the 28 μm PVDF film as an electrical-mechanical conversion layer, two 6 μm Ag layers as electrodes, and two 70 μm polyimide layers as encapsulations. Combining AH and the piezoelectric sensor, TPSS could seamlessly adhere to biological tissues. The fully encapsulated TPSS was small (30✗15✗0.2 mm^3), light (0.171 g), and flexible (Figure 1f–i). All these features ensure that TPSS work steadily in vivo while reducing damage to surrounding tissues.

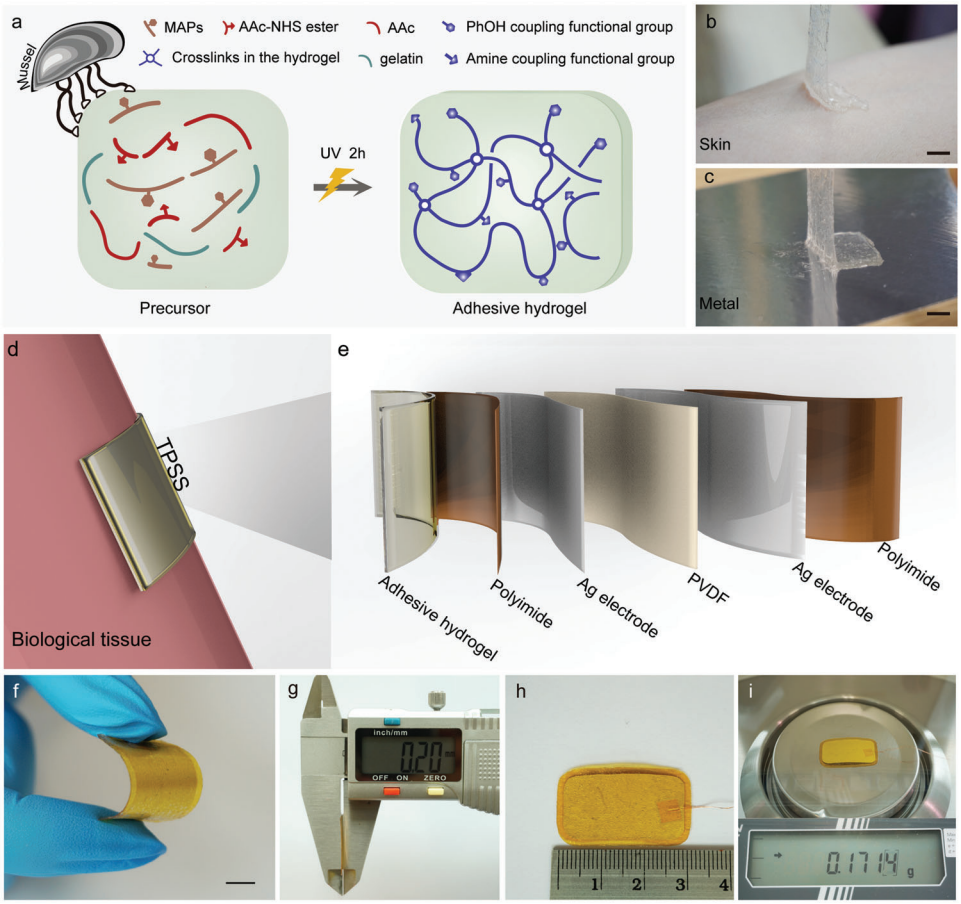

Figure 1. The overview of TPSS. a) The design process, components, and structure of AH. b) The AH adhered to the skin. c) The AH adhered to metal (Al film). Scale bars in (b) and (c) both are 1 cm. d) The diagram of TPSS in vivo, with the help of the AH, the TPSS anchor at the implant site. e) An exploded view of TPSS. f–i) The optical images of the TPSS in well flexible with a dimension of 30✗15✗0.2 mm^3, and a weight of 0.171 g. Scale bar: 1 cm.

2.2. The Adhesion Performance of AH

To evaluate the adhesion performance of AH with various targets, we conducted three different mechanical tests, measuring interfacial toughness by 180° peel test, shear strength by lap-shear test, and tensile strength by tensile test. To give a clear understanding, we detail displayed the test procedures of one group sample (AH and kidney). **Figure 2**a shows the optical photographs and force-displacement curve of the 180° peel test. The force increased with the displacement to peak and then decreased, stopped when the kidney sheets were completely separated. The interfacial toughness was calculated according to Equation (1), where F_{it} is the peak value of peel force, and W is the width of the AH. The test procedure and calculation method of shear strength was shown in Figure 2b. The force-displacement curve performed a similar tendency, with the peak appearing when two sheets were going to separate. The shear strength was calculated following Equation (2), where the F_{ss} is the peak value of measured force and L is the length of AH. Figure 2c demonstrated the tensile strength test procedure and corresponding curve, where two T-shaped 3D printing molds were used to assist testing. The peak value was higher than the previous two because it needs more energy to tear AH in a vertical direction. The tensile strength was calculated from Equation (3), where F_{ts} is the peak value of the measured force

$$\text{Interfacial toughness} = \frac{2F_{it}}{W} \tag{1}$$

$$\text{Shear strength} = \frac{F_{ss}}{WL} \tag{2}$$

$$\text{Tensile strength} = \frac{F_{ts}}{WL} \tag{3}$$

The strong adhesion mainly came from multiple interactions forming between AH and the targets' surface, including hydrogen bonds, covalent bonds as well as π–π interactions and charge–charge interactions. These interactions were contributed by various polar groups, like catechol groups, carboxyl groups, and NHS ester groups from AH (Figure 2d).[25,26] Fourier transform infrared (FTIR) results further verified ours suppose, as shown in Figure S4 (Supporting Information). The C–O stretch at 1087 cm^{-1} might come from catechol groups of MAPs, the sharp peak located at 1747 cm^{-1} indicated carboxylic acid C=O stretch, the symmetric C–N–C stretch located at 1201 cm^{-1} and asymmetric C–N–C stretch at 1297 cm^{-1} were related to

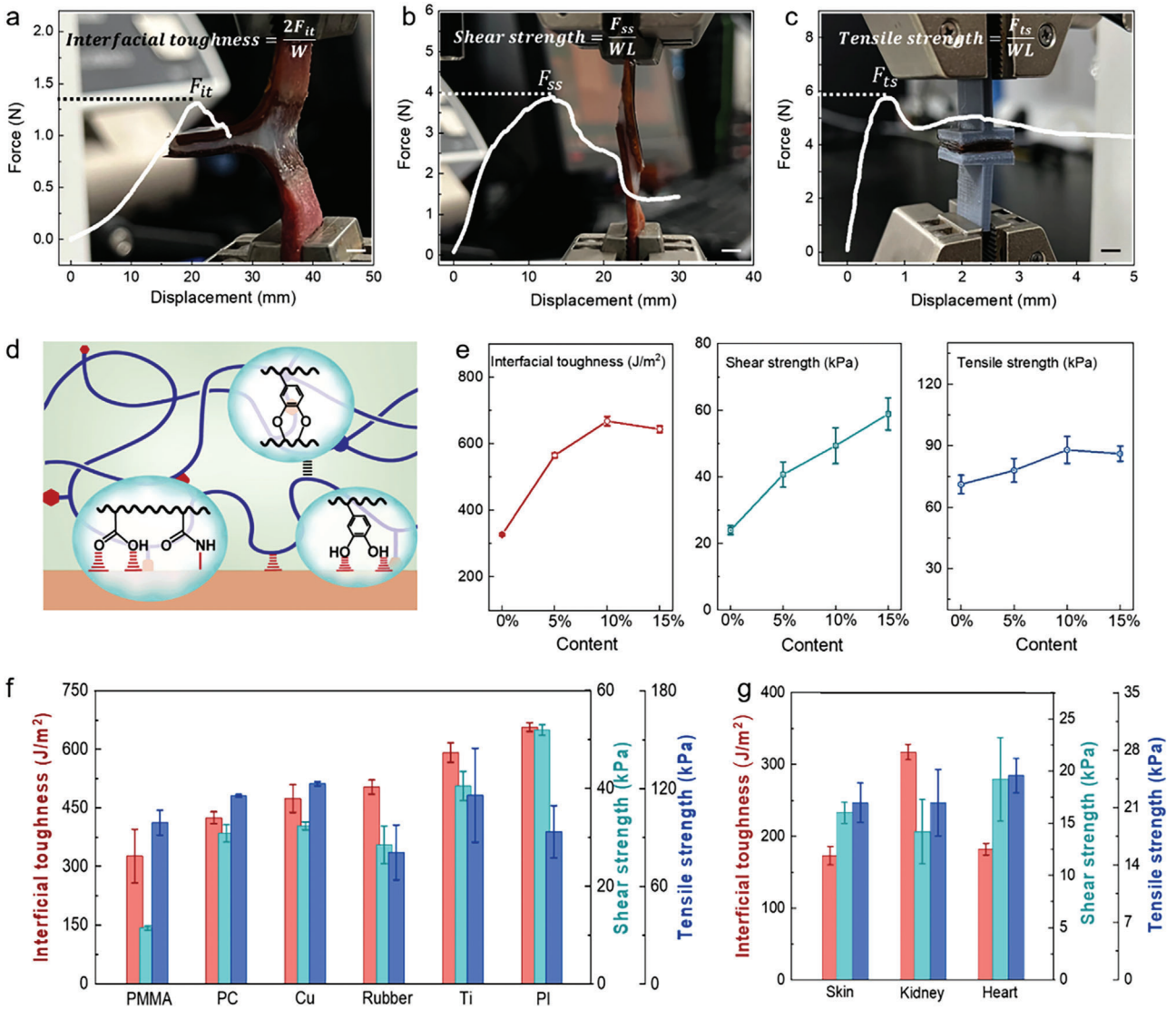

Figure 2. Mechanical adhesion performance of AH. The adhesion abilities of AH were evaluated by three methods: a) interfacial toughness tested by a standard 180° peel test, b) shear strength tested by a standard lap-shear test, and c) tensile strength tested by a standard tensile test. The biological targets used in (a–c) were small pieces of the kidney. Scale bar in (a-c) is 1 cm. d) The adhesion principle of AH. e) The interfacial toughness, shear strength, and tensile strength of AH (with PI as test targets) vary with the content of MAPs. f) Interfacial toughness, shear strength, and tensile strength between AH and various engineering materials. g) Interfacial toughness, shear strength, and tensile strength between AH and biological tissues. The loading speed of all tests was 30 mm min^{-1}.

NHS ester.[26,27] The adhesion performance of adhesive hydrogel could be optimized by tuning the content of MAPs. With MAPs content increased, the shear strength and tensile strength showed a rising tendency. The interfacial toughness increased from 327 to 667 J m^{-2} and then reduced to 643 J m^{-2}. The downward tendency may be due to more catechol groups participating in forming intramolecular interactions rather than contributing to surface adhesion. More details about mechanical tests of adhesive hydrogels with various MAPs contents could be found in Figure S5 (Supporting Information). Therefore, the AH with 10% MAPs was used for further study (unless otherwise specified, AH refers to samples containing 10% MAPs).

The mechanical adhesion between AH and other targets was systematically evaluated following the same procedures, including six commonly used engineering materials (PI, rubber, PC, PMMA, Ti, and Cu) and three biological tissues (skin, kidney, and heart). The optical images taken during the test procedure demonstrated the tightly adhesive interfaces, as shown in Figure S6 (Supporting Information). The corresponding force-displacement curves were recorded and summarized in Figure S7 (Supporting Information). Among these engineering materials, AH performed strong adhesion to PI with interfacial toughness of 656 J m^{-2}, shear strength of 51.9 kPa, and tensile strength of 93.6 kPa. Therefore, we chose PI as the packaging material for TPSS. Among biological tissues, the adhesion

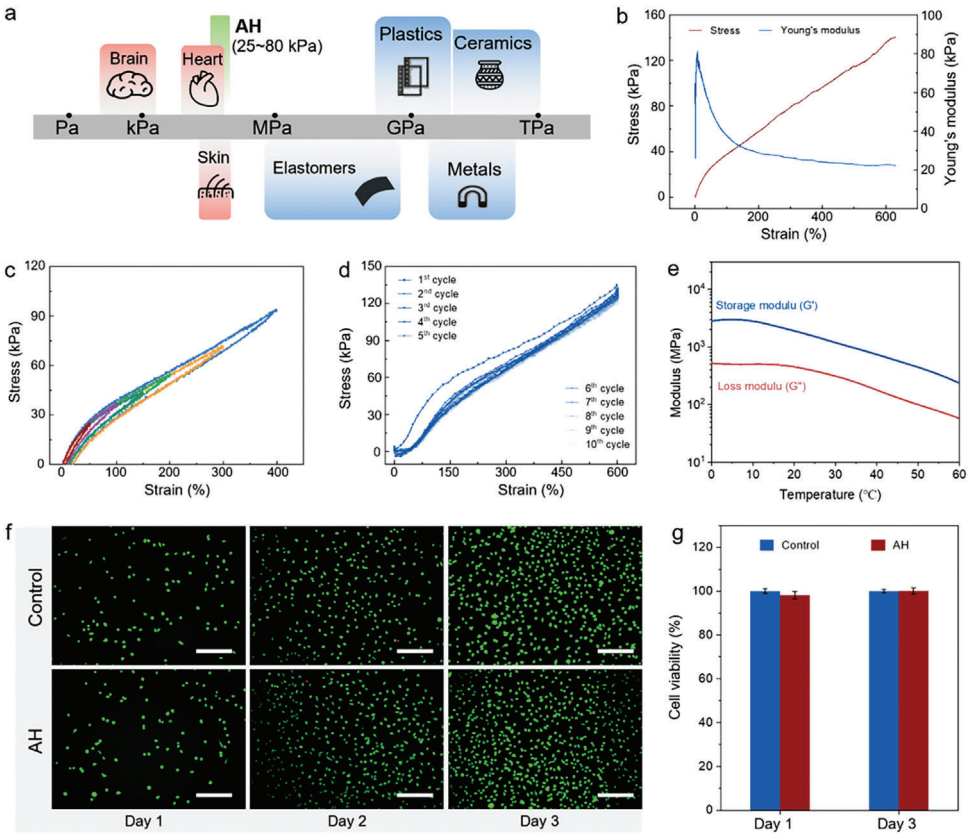

Figure 3. The mechanical performance and biocompatibility of AH. a) Young's modulus of AH is in the range of ≈25–80 kPa, which is located between engineering materials and biological tissues. b) The tensile strain-stress curve and Young's modulus curve of AH. c) The loading-unloading tensile strain–stress curves of AH with maximum tensile deformation fixed at 50%, 100%, 150%, 200%, 300%, and 400%. d) The 10 times loading–unloading tensile strain–stress curves of AH with maximum tensile deformation fixed at 400%. Loading speed in (c) and (d) was 30 mm min^{-1}. e) The storage modulus (*G'*) and loss modulus (*G''*) of AH under temperatures ranging from 0 to 60 °C. f) The fluorescence images and g) cell viability of stained mouse embryo fibroblasts after being cultured with AH for 1, 2, and 3 days. The scale bar in (f) is 200 µm.

ability showed increased tendency with skin, kidney, and heart. Compared with other similar works, the adhesion forming of AH does not require surface polar treatment of targets in advance, which is more efficient in real clinical application scenarios.

2.3. The Mechanical Softness and Biocompatibility of AH

The tissue-matched mechanical softness, including Young's modulus and stretchability, helps alleviate the foreign-body response of organisms.[19a] The Young's modulus of AH was ranging from 25 to 80 kPa, which was roughly placed between biological systems and engineering systems (**Figure 3**a,b).[19a] The breaking elongation and breaking tensile strength of AH were calculated as 631% and 140 kPa. Furtherly, the stress–strain curves of the hydrogels with different MAPs content (0%, 5%, 10%, and 15% by mass) were tested and displayed in Figure S8 (Supporting Information). The breaking elongation and max Young's modulus decreased along with the MAPs increased from 0% to 15%, while the tensile strengths (under the same strain) performed the opposite tendency. This may be because MAPs contributed to forming more dynamic interactions, which consumed energy by breaking and reconstructing bonds to protect the hydrogel film from fracture, while also sacrificing part strength.[23c]

To evaluate the recoverability of AH after stretching, we conducted the loading–unloading cycle test. The fusiform hysteresis loops were observed, which came from energy dissipation during tensile deformation (Figure 3c). When the applied tensile strain was 50% and 100%, the AH almost completely recovered to its original state after unloading. When the applied tensile strain was 150%, 200%, 300%, and 400%, there was less than 10% irreversible deformation remaining. Furthermore, 10 cycles loading–unloading test demonstrated the stability of AH under 600% tensile deformation (Figure 3d). After the first cycle, the loading and unloading curves almost overlapped, indicating less energy dissipation. This behavior was mainly related to the arranged polymer segments following the stretching direction. The storage modulus (*G'*) kept larger than the loss modulus (*G''*) under temperatures from 0 to 60 °C, indicating the stable solid state of AH (Figure 3e; and Figure S9, Supporting Information). This is important for implants to keep stable functions given the temperature differences between the in vivo and in vitro environments. Good biocompatibility is essential to reduce foreign-body reactions and subsequent adverse effects on the organism. After being cultured with an AH-contained medium for 1, 2, and

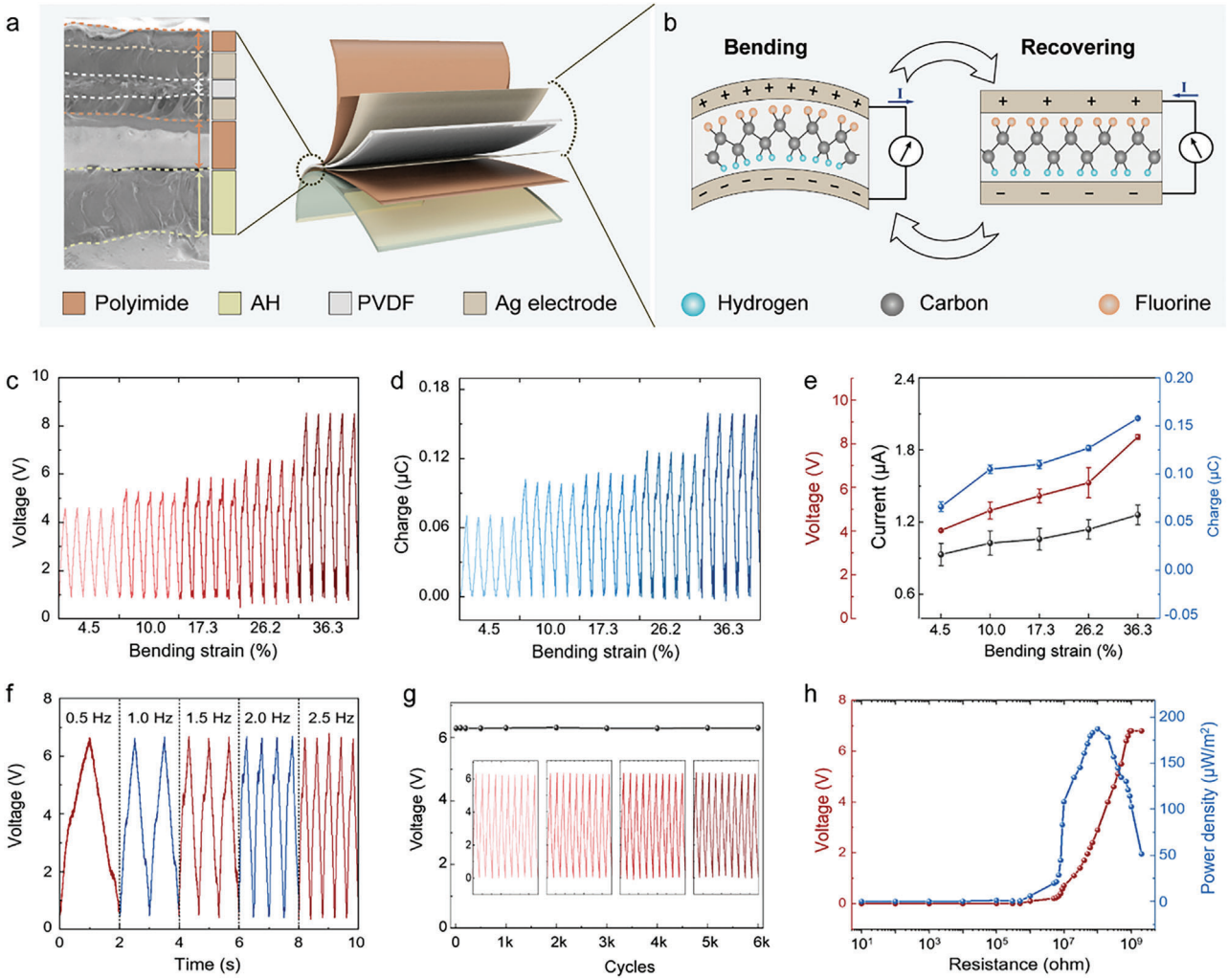

Figure 4. In vitro electrical performance of TPSS. a) The SEM and explosive view of TPSS displayed the multi-layered structure with close contact between layers. b) The working principle of TPSS. c) The V_{oc} and d) C_{sc} of TPSS under different bending strains. e) The V_{oc}, I_{sc}, and C_{sc} of TPSS vary with different bending strains. f) The V_{oc} of TPSS under different frequencies with the bending strain fixed at 26.2%. g) The V_{oc} and power density of TPSS in an impedance-matching test. h) The performance stability of TPSS with 6000 times bending-recovering test under the 26.2% bending strain.

3 days, the Mouse fibroblasts L929s showed normal adherence behavior and cell morphology (Figure 3f; and Figure S10, Supporting Information). The cell viability of both experimental and control groups was near 100% after 3 days, which indicates the good biocompatibility of AH (Figure 3g). In conclusion, with the advantages of tissue-similar mechanical softness, tissue-matched Young's modulus, and good biocompatibility, AH demonstrated its potential in bridging biological tissues and implantable bioelectronics.

2.4. The In Vitro Electrical Performance of TPSS

The tissue-adhesive piezoelectric soft sensor was constructed with PVDF as a mechanical-electrical conversion unit, Ag as electrodes, PI as packaging layers, and AH as a tissue-attaching layer. **Figure 4**a; and Figure S11 (Supporting Information) demonstrated the multilayer structure of TPSS and the close adhesion between layers. The detailed working principle of TPSS was demonstrated in Figure 4b, which is based on the positive piezoelectric effect of PVDF in the β phase. When TPSS was bending pressed by external mechanical movements, the polarized dipole density of PVDF film increased correspondingly. At the same time, electrons flowed from the bottom electrode to the top electrode through an external circuit to keep charge balance. After removing external force, TPSS returned to its original state. Polarized dipole density decreased, and electrons flowed from the top electrode to the bottom electrode. By connecting the display system to the external circuit, the alternating electrical signals could be read out. An element simulation was conducted to verify the surface potential distribution of TPSS using COMSOL Multiphysics. There was almost no obvious difference in surface potential distribution between the simulation models with an AH layer and without AH payer (Figure S12, Supporting Information).

During in vitro electrical performance studies, a linear motor was used to drive TPSS to generate bending strain along the Z

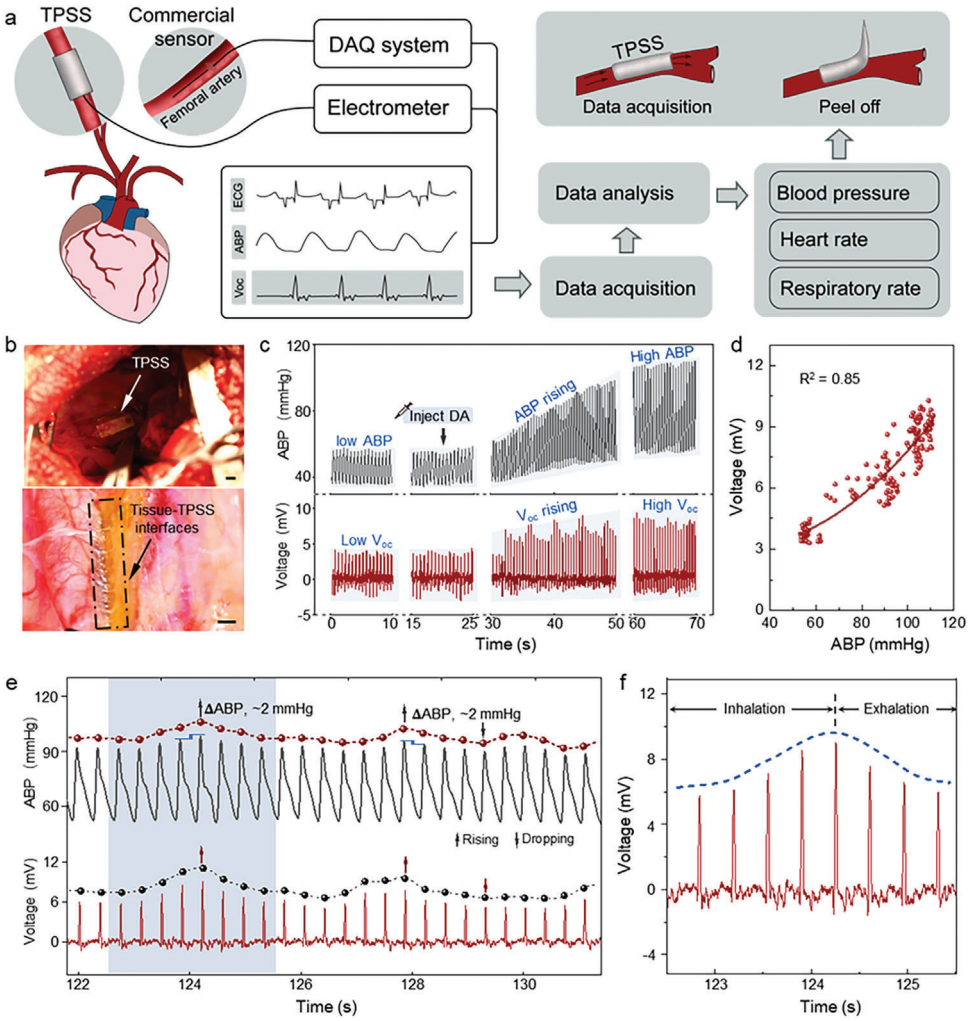

Figure 5. The in vivo sensing performance of TPSS. a) Schematic diagram of in vivo experimental test system. b) TPSS is closely attached to the surface of the right-side internal carotid artery. Scale bar: 1 cm. c) The blood pressure date from a commercial sensor (top) and the corresponding output signals from TPSS (down). d) The relationship between the arterial blood pressure and the output voltage of TPSS. e) V_{oc} of TPSS can sensitively distinguish the slight rising or dropping of ABP. f) The overall uptrend and downtrend of voltage peaks are caused by inhalation and exhalation movements.

axis, which direction has the highest piezoelectric response. We defined the bending strain of TPSS in Figure S13 and Table S2 (Supporting Information). The open-circuit voltage (V_{oc}), short-circuit current (I_{sc}), and short-circuit charge (Q_{sc}) of TPSS under various bending strains were tested and summarized in Figure 4c–e; and Figure S14 (Supporting Information). Under 4.5%, 10.0%, 17.3%, 26.2%, and 36.3% bending strain, the V_{oc} was 4.02, 4.93, 5.6, 6.2, and 8.3 V, respectively. Correspondingly, the Q_{sc} was 0.07, 0.105, 011, 0.127, and 0.158 μC as well as the I_{sc} was 0.93, 1.03, 1.059, 1.14, and 1.26 μA. The test frequency showed less effect on the output performance of TPSS. Keeping bending strain as 26.2%, the V_{oc} of TPSS was calculated as 6.54, 6.49, 6.58, 6.59, and 6.50 V under 0.5, 1.0, 1.5, 2.0, and 2.5 Hz test frequency (Figure 4f). As an implantable pressure sensor, keeping working performance stable is essential. We evaluated the cycle stability of TPSS under 26.2% bending strain with a test frequency fixed at 1 Hz. After 6000 times bending and recovering tests, there was almost no attenuation with the V_{oc} of TPSS kept stable around 6.3 V (Figure 4g). The energy output of TPSS could be maximized by conducting an impedance-matching experiment. As shown in Figure 4h, the power density reached a peak of 186.9 μW m^{-2} with an external resistance of 10^8 Ω, which was matched with the internal impedance of TPSS.

2.5. In Vivo Sensing Performance

To evaluate the in vivo performance of TPSS, an adult Yorkshire porcine (about 40 kg) was employed in this work. **Figure 5**a schematic demonstrated the test system used in this animal model. The TPSS was seamlessly attached to the right-side internal carotid artery, which was linked with an electrometer. In parallel, a commercial sensor was used as a reference, which worked by inserting a probe into the femoral artery. The data acquisition (DAQ) system was employed to display the arterial blood pressure (ABP) and electrocardiograph (ECG) from commercial sensors. As a pressure sensor, TPSS captured the mechanical physiological movement of biological tissue and

converted it into visible electrical signals. By collecting and analyzing these alternating electrical signals, we could monitor intraoperative blood pressure, heart rate, and respiratory rate. Based on the mechanical flexibility and strong tissue-adhesive ability of AH, TPSS closely adhered to the surface of biological tissues. Moreover, after completing the service, TPSS was easily peeled off from the tissue. Figure 5b shows the close interfaces between TPSS and the internal carotid artery.

The pressure from blood flow in the internal carotid artery drove TPSS to deform and output electrical signals. After injecting dopamine (DA), ABP slowly rose from 55 mmHg (low ABP area) to 110 mmHg (high ABP area), and the V_{oc} of TPSS increased correspondingly (Figure 5c). The real-time ABP and the V_{oc} of TPSS satisfied the fitting equation $Y = 3.5–0.039\,X + 8.2E^{-4}\,X^2$, where X referred to artery blood pressure, Y referred to the peak value of V_{oc}, R^2 was calculated as 0.85 (Figure 5d). Furthermore, the TPSS accurately distinguished the slight rise and drop of ABP, even 2 mmHg, which demonstrated outstanding sensing performance (Figure 5e). At the same time, we noticed that the periodic fluctuations of both ABP and V_{oc} were related to the breathing movements of the experimental animal. During inhalation, the ABP and V_{oc} kept rising, which was opposite to that during exhalation. As shown in Figure S15a,b (Supporting Information), the real-time respiratory rate was calculated as about 14 cycles per minute (cpm) according to the time of one inhalation/exhalation cycle displayed in the V_{oc} curve. A similar periodic relationship could be found between the peak of V_{oc} curves and the R wave in electrocardiogram (ECG), as shown in Figure S15c,d (Supporting Information). The real-time heart rate was calculated as 130 beats per minute (bpm) through the peak-to-peak time interval of V_{oc} from TPSS, which is close to that calculated from ECG. As a control group, a piezoelectric sensor without AH layer was implanted into the same site (Figure S16a,b, Supporting Information). As shown in Figure S16c (Supporting Information), the waveform had no characteristic peaks and showed little variation in amplitude, which indicated ineffective contact between the piezoelectric sensor and artery. In general, with AH as a tissue-adhesive layer, TPSS formed nondamaging, seamless, and effective communications with the artery. Meanwhile, the output performance of TPSS was closely related to artery blood pressure, respiration rate, and heart rate, demonstrating its great potential for monitoring cardiovascular health status.

3. Conclusions

In conclusion, this work proposed an implantable tissue-adhesive piezoelectric soft sensor, which demonstrated their potential for monitoring in vivo intraoperative vital indicators. First, inspired by the adhesive behavior of mussels in seawater, we designed the adhesive hydrogel (AH) based on biologically derived MAPs and gelatin through polymerization under UV light. The optimized AH with 10% MAPs performed superior mechanical adhesion with six commonly used engineering materials (PI, rubber, PC, PMMA, Ti, and Cu) and three biological tissues (kidney, skin, and heart). AH was able to withstand over 631% tensile deformation with the corresponding breaking strength of 140 kPa. The Young's module of AH was calculated ranging from 28 to 80 kPa, which is well-matched biological tissue. Taking all advantages of tissue-similar mechanical softness, tissue-matched Young's modulus, good biocompatibility, and strong adhesion to both organic and inorganic interfaces, AH proved to be a strong candidate in human–machine interfaces. TPSS demonstrated good in vitro electrical performance with a high output of 8.3 V, long-term stability of over 6000 cycles, and high energy power density of 186.9 μW m^{-2}. In a large animal experiment, TPSS proved its in vivo application potential as a self-powered pressure sensor for monitoring blood pressure, heart rate, and respiratory rate during surgery. Compared to commercial sensors that worked by inserting into tissues, TPSS did not cause any damage and could be peeled off after service. The integration of adhesive hydrogel and self-powered pressure sensor enabled the biocompatible, seamless, and more efficient interactions between the biological system and iBEDs, which also provided reference to next-generation implantable bioelectronics with features of battery-free, intelligent, and accurate.

4. Experimental section

Materials: All chemicals were used without further purification. To prepare the adhesive hydrogel, the mussel adhesive proteins (MAPs, Usun Bio), acrylic acid (AA, Sigma-Aldrich), gelatin from porcine skin (Sigma-Aldrich), *N*-hydroxysuccinimide ester (AAc-NHS ester, Sigma-Aldrich, CAS 38862-24-7), α-ketoglutaric acid (Sigma-Aldrich), gelatin methacryloyl from porcine skin with strength bloom 90–110 g and degree of substitution 60% (GelMa, Sigma-Aldrich) were used. The PI, Ti, rubber, Cu, PC, PMMA film, and tissues were purchased from Casmart. L929 cells (fibroblasts, GNM28) were from the Cell Bank of the Chinese Academy of Sciences in Beijing, China. Phosphate buffer saline (PBS), Calcein-AM/PI Live/Dead double-labeled kit, and Cell Count Kit-8 (CCK-8) was purchased from Beijing Solarbio Technology Co., Ltd. Piezoelectric film, polyimide type, and Cu wire was purchased from TE Connectivity.

Characterization: A transmission Fourier transform infrared spectroscope (VERTEX80v, Bruker) was used to characterize the chemical composition of AH with wave numbers ranging from 400 to 5000 cm^{-1}. The morphology of AH and TPSS were observed by Hitachi field emission SEM (SU 8020, Hitachi). The dynamic mechanical analysis (DMA) was conducted in the air atmosphere (Q800, TA Instruments) with an AH dimension of 6.5✗5.0✗0.52 mm^3. With a tensile preload force of 0.01 N, the small oscillations of amplitude 1% strain were applied at 1 Hz frequency. The temperature sweeps from 0 to 60 °C were performed at a rate of 5 °C min^{-1}. The potential distribution of the TPSS under the bending state was analyzed through a finite element simulation using COMSOL Multiphysics.

Preparation of Adhesive Hydrogels: To prepare the adhesive hydrogel with 5% mussel adhesive protein (by mass ratio to water), 0.5 g MAPs, 3.0 g acrylic acid, 1.0 g gelatin from porcine skin, 0.1 g *N*-hydroxysuccinimide ester, 0.01 g gelatin methacryloyl, and 0.02 g α-ketoglutaric acid were dissolved in 10.0 mL deionized water through continuous magnetic stirring for 2 h. The as-prepared mixture was filtered with 0.4 μm sterile syringe filters and transferred to the 10✗10 cm^2 glass mold with 210 μm spacer. After 2 h curing under ultraviolet light (UV, 365 nm, 20 W), the adhesive hydrogel was got. The adhesive hydrogel with 10% and 15% MAPs were prepared by adding 1.0 and 1.5 g MPA, respectively.

Preparation of TPSS: The as-fabricated pressure sensor consisted of a piezoelectric layer, electrodes, packaging layers, and an adhesive layer. In detail, the commercial piezoelectric film with a total thickness of 40 μm was cut into 1.5✗3.0 cm^2. Wiping four edges of the piezoelectric film with acetone to avoid conduction between two electrodes. Both electrodes need to be linked with short Cu wires with the help of silver paste. The polyimide type was attached on both sides of the PVDF film as packaging layers. After attaching the adhesive hydrogel in thickness of about 200 μm on one side of the as-fabricated device, the TPSS was got.

Stretchability and Young's Modulus Evaluation of AH: To explore the stretchability and Young's modulus of the as-fabricated hydrogel, an electrical vertical test bench (Mark-10/ESM301) was used for uniaxial tensile test, and a force gauge (Mark 10/M5) was used to detect real-time tensile force. To explore the recovery after 50%, 100%, 150%, 200%, 300%, and 400% tensile stretchability, 10 times cycle uniaxial tensile test was conducted. For all uniaxial tensile tests, the tensile loading speed was 30 mm min^{-1}. All samples were in sizes of 30✗10✗1 mm^3. The tensile strain, tensile strength, and Young's modulus of AH were calculated by Equations (4), (5), and (6), respectively

$$\varepsilon = \frac{L - L_0}{L_0} \times 100\% \tag{4}$$

$$\delta = \frac{F}{S} \tag{5}$$

$$E = \frac{\delta}{\varepsilon} \tag{6}$$

Where ε is the tensile strain, δ is the tensile strength, E is Young's modulus, L is the length of the tested sample after tensile stretching, L_0 is the original length of the sample, F is the tensile force, S is the cross-sectional area of the tested sample.

Adhesion of AH: Interfacial toughness between AH and targets was tested by standard 180° peel test (ASTM F2256).[26] Shear strength between AH and targets was tested by a standard lap-shear test (ASTM F2255). Tensile strength between AH and targets was tested by standard tensile test (ASTM F2258). All adhesion tests were conducted by Mark-10/MSE 301/M5 with a constant peeling speed of 30 mm min^{-1}.

Biocompatibility test of AH: The AH-conditioned medium for cell culture was prepared by incubating 100 mg sterilized AH in 50 mL standard Dulbecco's modified Eagle's medium (DMEM, Gibco) at 37 °C for 24 h. The L929 cells were seeded in a 24-well cell culture plate ($n = 10$ for AH-conditioned medium as the experimental group and $n = 10$ for pristine DMEM as the control group). The L929 cells were cultured for 1 d, 2 d, and 3 d at 37 °C under 95% air and 5% CO^2. To observe cell morphology, the L929 cells at 1, 2, and 3 d were immunofluorescent stained using the Calcein-AM/PI Live/Dead double-labeled kit. The immunofluorescence images of cells were acquired by an inverted fluorescence microscope (DM6000, Leica) under 490±10 nm (live) and 545 nm (dead). To quantify the cell viability, 10% CCK-8 solution and 90% culture medium were used to treat L929 cells for 2 h after washing the cells with 1✗PBS. Then, 200 µL supernatant of each well was transferred into a 96-well plate. The absorbance of the solution was measured under 450 nm with a microplate absorbance assay instrument.

In vitro electrical test of TPSS: The V_{oc} was acquired by an oscilloscope (Teledyne LeCroy DPO6450), and the I_{sc} and Q_{sc} were acquired using an electrometer (Keithley 6517). A linear motor (LinMot E1100) was used to explore the electrical output under periodic tensile loads. The 6000-times fatigue test was conducted under 1 Hz and 150° bending strain. All devices used in vitro electrical test were in dimensions of 30✗15✗0.8 mm^3.

In vivo study: The animal experiment was performed by the Nongnong (Beijing) Life & Technology Company and approved by the Ethical Committee of Animal Experimental Center. The adult male Yorkshire pig (≈40 kg) fasted for 12 h before surgery. After that, the animal was anesthetized by intravenous injection of propofol (6 mg kg^{-1}) and maintained on 1–3% isoflurane with positive-pressure ventilation. The right-side internal carotid artery was exposed with an incision. Then, the TPSS with the dimensions of 30✗15✗0.6 mm^3 was adhered to the artery and connected to an oscilloscope to acquire and record real-time electrical signals. An arterial pressure catheter was inserted into the right femoral artery and connected with the DAQ system (PowerLab 4/35) to record blood pressure. Three probes were fixed on the limbs of the animal and connected to the DAQ system to record ECG.

Supporting Information

Supporting Information is available from the Wiley Online Library or from the author.

Acknowledgements

This work was supported by the National Key Research and Development Program of China (No. 2022YFE0111700), the Fundamental Research Funds for the Central Universities (No. E0EG6802 × 2), the National Natural Science Foundation of China (Nos. T2125003, 82102231, and 82100325), the Beijing Natural Science Foundation (Nos. JQ20038 and L212010), The Beijing Gold-bridge project (No. ZZ21055), National Science and Technology project of Wenxin Granule Phase IV clinical study (No. 2013-ZDZX01-P), the Reimagine Research Scheme (RRSC) grant (Scalable AI Phenome Platform towards Fast-Forward Plant Breeding (Sensor), Project Nos. A-0009037-02-00 & A0009037-03-00) at NUS, Singapore; the Reimagine Research Scheme (RRSC) grant (Under-utilized Potential of Microbiomes (soil) in Sustainable Urban Agriculture).

Conflict of Interest

The authors declare no conflict of interest.

Author Contributions

C.W., Y.H., and Y.L. contributed equally to this work. C.L., Z.L., and Z.L. proposed and supervised the project. C.W. and Y.L. carried out synthesis, characterizations, and data collection. C.W. and Y.L. carried out AH fabrication and characterization. Y.S. carried out the cell experiment. C.W., Z.L., Y.H., Y.L., S.C., W.H., and X.Q. carried out the animal experiment. J.X. carried out COMSOL Stimulation. C.W., H.Z., W.L., Z.G. carried out the FTIR, SEM, optical images of device. C.W., Y.T., Z.L., Z.L., and C.L. oversaw the paper with edits from all authors. All the authors discussed the results and commented on the manuscript and have given approval to the final version of the manuscript.

Data Availability Statement

Research data are not shared.

Keywords

adhesive hydrogels, blood pressures, device-tissue interfaces, mussel adhesive protein, piezoelectric

Received: April 3, 2023
Revised: May 8, 2023
Published online:

[1] a) R. Feiner, T. Dvir, *Nat. Rev. Mater.* **2018**, *3*, 17076; b) M. Lin, H. Hu, S. Zhou, S. Xu, *Nat. Rev. Mater.* **2022**, *7*, 850; c) F. Yang, J. Li, Y. Long, Z. Zhang, L. Wang, J. Sui, Y. Dong, Y. Wang, R. Taylor, D. Ni, W. Cai, P. Wang, T. Hacker, X. Wang, *Science* **2021**, *373*, 337; d) W. Deng, Y. Zhou, A. Libanori, G. Chen, W. Yang, J. Chen, *Chem. Soc. Rev.* **2022**, *51*, 3380; e) D. Huang, Y. Cheng, G. Chen, Y. Zhao, *Research* **2023**, *6*, 0022; f) K. Meng, S. Zhao, Y. Zhou, Y. Wu, S. Zhang, Q. He, X. Wang, Z. Zhou, W. Fan, X. Tan, J. Yang, J. Chen, *Matter* **2020**, *2*, 896;

g) Y. Luo, M. R. Abidian, J. H. Ahn, D. Akinwande, A. M. Andrews, M. Antonietti, Z. Bao, M. Berggren, C. A. Berkey, C. J. Bettinger, J. Chen, P. Chen, W. Cheng, X. Cheng, S. J. Choi, A. Chortos, C. Dagdeviren, R. H. Dauskardt, C. A. Di, M. D. Dickey, et al., *ACS Nano* **2023**, *17*, 5211.

[2] a) Y. Jiang, S. Ji, J. Sun, J. Huang, Y. Li, G. Zou, T. Salim, C. Wang, W. Li, H. Jin, J. Xu, S. Wang, T. Lei, X. Yan, W. Y. X. Peh, S. C. Yen, Z. Liu, M. Yu, H. Zhao, Z. Lu, G. Li, H. Gao, Z. Liu, Z. Bao, X. Chen, *Nature* **2023**, *614*, 456; b) R. Wang, J. Sui, X. Wang, *ACS Nano* **2022**, *16*, 17708.

[3] a) X. Chen, B. Assadsangabi, Y. Hsiang, K. Takahata, *Adv. Sci.* **2018**, *5*, 1700560; b) J. Li, T. A. Hacker, H. Wei, Y. Long, F. Yang, D. Ni, A. Rodgers, W. Cai, X. Wang, *Nano Energy* **2021**, *90*, 106507.

[4] a) H. Ouyang, Z. Li, M. Gu, Y. Hu, L. Xu, D. Jiang, S. Cheng, Y. Zou, Y. Deng, B. Shi, W. Hua, Y. Fan, Z. Li, Z. Wang, *Adv. Mater.* **2021**, *33*, 2102302; b) Y. S. Choi, H. Jeong, R. T. Yin, R. Avila, A. Pfenniger, J. Yoo, J. Y. Lee, A. Tzavelis, Y. J. Lee, S. W. Chen, H. S. Knight, S. Kim, H.-Y. Ahn, G. Wickerson, A. V. Guardado, E. Higbee-Dempsey, B. A. Russo, M. A. Napolitano, T. J. Holleran, L. A. Razzak, A. N. Miniovich, G. Lee, B. Geist, B. Kim, S. Han, J. A. Brennan, K. Aras, S. S. Kwak, J. Kim, E. A. Waters, X. Yang, et al., *Science* **2022**, *376*, 1006.

[5] a) F. R. Fan, Z. Q. Tian, Z. L. Wang, *Nano Energy* **2012**, *1*, 328; b) X. Guo, T. He, Z. Zhang, A. Luo, F. Wang, E. J. Ng, Y. Zhu, H. Liu, C. Lee, *ACS Nano* **2021**, *15*, 19054; c) X. Xia, Z. Zhou, Y. Shang, Y. Yang, Y. Zi, *Nat. Commun.* **2023**, *14*, 1023; d) H. J. Yoon, S. W. Kim, *Joule* **2020**, *4*, 1398; e) H. Shen, H. Lei, M. Gu, S. Miao, Z. Gao, X. Sun, L. Sun, G. Chen, H. Huang, L. Chen, Z. Wen, *Adv. Funct. Mater.* **2022**, *32*, 2204525; f) J. Jiang, X. Sun, Z. Wen, *Adv. Sensor Res.* **2022**, *1*, 2200011; g) J. Liu, Z. Wen, H. Lei, Z. Gao, X. Sun, *Nanomicro Lett.* **2022**, *14*, 88.

[6] Q. Li, Z. Li, J. Meng, *I. J. Optomechatronics* **2022**, *16*, 1.

[7] Q. Zheng, B. Shi, F. Fan, X. Wang, L. Yan, W. Yuan, S. Wang, H. Liu, Z. Li, Z. L. Wang, *Adv. Mater.* **2014**, *26*, 5851.

[8] Z. Li, G. Zhu, R. Yang, A. C. Wang, Z. L. Wang, *Adv. Mater.* **2010**, *22*, 2534.

[9] a) Q. Zheng, Y. Zou, Y. Zhang, Z. Liu, B. Shi, X. Wang, Y. Jin, H. Ouyang, Z. L. Li, Z. L. Wang, *Sci. Adv.* **2016**, *2*, e1501478; b) D. M. Lee, N. Rubab, I. Hyun, W. Kang, Y. J. Kim, M. Kang, B. O. Choi, S. W. Kim, *Sci. Adv.* **2022**, *8*, eabl8423; c) W. Jiang, H. Li, Z. Liu, Z. Li, J. Tian, B. Shi, Y. Zou, H. Ouyang, C. Zhao, L. Zhao, R. Sun, H. Zheng, Y. Fan, Z. L. Wang, Z. Li, *Adv. Mater.* **2018**, *30*, 1801895.

[10] a) I. M. Imani, B. Kim, X. Xiao, N. Rubab, B. J. Park, Y. J. Kim, P. Zhao, M. Kang, S. W. Kim, *Adv. Sci.* **2023**, *10*, 2204801; b) G. Wang, H. Feng, L. Hu, W. Jin, Q. Hao, A. Gao, X. Peng, W. Li, K. Y. Wong, H. Wang, Z. Li, P. K. Chu, *Nat. Commun.* **2018**, *9*, 2055.

[11] a) C. Chen, Z. Wen, J. Shi, X. Jian, P. Li, J. T. W. Yeow, X. Sun, *Nat. Commun.* **2020**, *11*, 4143; b) H. Ryu, H. M. Park, M. K. Kim, B. Kim, H. S. Myoung, T. Y. Kim, H. J. Yoon, S. S. Kwak, J. Kim, T. H. Hwang, E. K. Choi, S. W. Kim, *Nat. Commun.* **2021**, *12*, 4374; c) R. H. Hinche, H. J. Yoon, H. Ryu, M. K. Kim, E. K. Choi, D. S. Kim, S. W. Kim, *Science* **2019**, *365*, 491.

[12] Z. Liu, Y. Ma, H. Ouyang, B. Shi, N. Li, D. Jiang, F. Xie, D. Qu, Y. Zou, Y. Huang, H. Li, C. Zhao, P. Tan, M. Yu, Y. Fan, H. Zhang, Z. L. Wang, Z. Li, *Adv. Funct. Mater.* **2019**, *29*, 1807560.

[13] H. Ouyang, Z. Liu, N. Li, B. Shi, Y. Zou, F. Xie, Y. Ma, Z. Li, H. Li, Q. Zheng, X. Qu, Y. Fan, Z. L. Wang, H. Zhang, Z. Li, *Nat. Commun.* **2019**, *10*, 1821.

[14] a) J. Wang, H. Wang, T. He, B. He, N. V. Thakor, C. Lee, *Adv. Sci.* **2019**, *6*, 1900149; b) J. Wang, H. Wang, N. V. Thakor, C. Lee, *ACS Nano* **2019**, *13*, 3589; c) Y. Cheng, Y. Xu, Y. Qian, X. Chen, Y. Ouyang, W. E. Yuan, *Nano Energy* **2020**, *69*, 104411; d) F. Jin, T. Li, T. Yuan, L. Du, C. Lai, Q. Wu, Y. Zhao, F. Sun, L. Gu, T. Wang, Z. Q. Feng, *Adv. Mater.* **2021**, *33*, 2104175.

[15] a) W. Xu, Z. Liu, X. Lu, J. Tian, G. Chen, B. Liu, Z. Li, X. Qu, C. Wen, *Sci. China Mater.* **2019**, *62*, 1053; b) Y. Zhang, L. Xu, Z. Liu, X. Cui, Z. Xiang, J. Bai, D. Jiang, J. Xue, C. Wang, Y. Lin, Z. Li, Y. Shan, Y. Yang, L. Bo, Z. Li, X. Zhou, *Nano Energy* **2021**, *85*, 106009.

[16] a) C. Zhao, H. Feng, L. Zhang, Z. Li, Y. Zou, P. Tan, H. Ouyang, D. Jiang, M. Yu, C. Wang, H. Li, L. Xu, W. Wei, Z. Li, *Adv. Funct. Mater.* **2019**, *29*, 1808640; b) E. O. Gabrielsson, Y. H. Jung, J. H. Han, D. J. Joe, D. T. Simon, K. J. Lee, M. Berggren, *Adv. Mater.* **2021**, *6*, 2100526.

[17] a) A. Borchers, T. Pieler, *Genes* **2010**, *1*, 413; b) Q. Zheng, B. Shi, Z. Li, Z. L. Wang, *Adv. Sci.* **2017**, *4*, 1700029.

[18] a) J. Li, L. Kang, Y. Yu, Y. Long, J. J. Jeffery, W. Cai, X. Wang, *Nano Energy* **2018**, *51*, 728; b) Y. Yu, H. Sun, H. Orbay, F. Chen, C. G. England, W. Cai, X. Wang, *Nano Energy* **2016**, *27*, 275.

[19] a) H. Yuk, J. Wu, X. Zhao, *Nat. Rev. Mater.* **2022**, *7*, 935; b) C. Sung, W. Jeon, K. S. Nam, Y. Kim, H. Butt, S. Park, *J. Mater. Chem. B* **2020**, *8*, 6624.

[20] J. Rogers, T. Someya, Y. Huang, *Science* **2010**, *327*, 1603.

[21] a) Y. Cong, J. Fu, *Langmuir* **2022**, *38*, 11503; b) J. Deng, H. Yuk, J. Wu, C. E. Varela, X. Chen, E. T. Roche, C. F. Guo, X. Zhao, *Nat. Mater.* **2021**, *20*, 229; c) D. Gan, Z. Wang, C. Xie, X. Wang, W. Xing, X. Ge, H. Yuan, K. Wang, H. Tan, X. Lu, *Adv. Healthcare Mater.* **2019**, *8*, 1901103.

[22] Y. Hou, Y. Li, Y. Li, D. Li, T. Guo, X. Deng, H. Zhang, C. Xie, X. Lu, *ACS Nano* **2023**, *17*, 2745.

[23] a) C. M. Tringides, N. Vachicouras, I. de Lazaro, H. Wang, A. Trouillet, B. R. Seo, A. Elosegui-Artola, F. Fallegger, Y. Shin, C. Casiraghi, K. Kostarelos, S. P. Lacour, D. J. Mooney, *Nat. Nanotechnol.* **2021**, *16*, 1019; b) F. Wu, J. Li, K. Zhang, Z. He, P. Yang, D. Zou, N. Huang, *ACS Appl. Mater. Interfaces* **2016**, *8*, 109; c) C. Wang, Y. Liu, X. Qu, B. Shi, Q. Zheng, X. Lin, S. Chao, C. Wang, J. Zhou, Y. Sun, G. Mao, Z. Li, *Adv. Mater.* **2022**, *34*, 2105416.

[24] a) Y. Liu, C. Wang, J. Xue, G. Huang, S. Zheng, K. Zhao, J. Huang, Y. Wang, Y. Zhang, T. Yin, Z. Li, *Adv. Healthcare Mater.* **2022**, *11*, e2200653; b) Z. Xiao, D. Wang, C. Wang, Z. Chen, C. Huang, Y. Yang, L. Xie, L. Zhang, L. Xu, M. R. Zhang, K. Hu, Z. Li, L. Luo, *Mater Today Bio* **2022**, *15*, 100297.

[25] a) B. Xue, J. Gu, L. Li, W. Yu, S. Yin, M. Qin, Q. Jiang, W. Wang, Y. Cao, *Nat. Commun.* **2021**, *12*, 7156; b) H. Lee, S. M. Dellatore, W. M. Miller, P. B. Messersmith, *Science* **2007**, *318*, 426.

[26] H. Yuk, C. E. Varela, C. S. Nabzdyk, X. Mao, R. F. Padera, E. T. Roche, X. Zhao, *Nature* **2019**, *575*, 169.

[27] A. Thakur, S. Ranote, D. Kumar, K. K. Bhardwaj, R. Gupta, G. S. Chauhan, *ACS Omega* **2018**, *3*, 7925.